Experiments in Fluids (2019) 60:169
https://doi.org/10.1007/s00348-019-2805-3

RESEARCH ARTICLE

Experimental investigation on water repellency and anisotropic wettability of microgrooved polymer surfaces

Daehee Kwon[1] · Sangmin Lee[2] · Eunseop Yeom[3]

Received: 1 July 2019 / Revised: 29 August 2019 / Accepted: 3 September 2019 / Published online: 28 October 2019
© Springer-Verlag GmbH Germany, part of Springer Nature 2019

Abstract

Simple patterns on a surface can enhance water repellency and simultaneously impose directional wettability. Surfaces exhibiting periodic microscale grooves are examples of such surfaces. Here, we design microgrooved surfaces with three different groove widths and experimentally investigate their impact behaviors on the surfaces. In terms of wetting state, the robustness of water repellency against an impinging droplet is evaluated. Contact angle of a surface alone cannot represent the water repellency against impinging droplets. Surfaces with large contact angles are found to be less water repellent. However, water repellency of a surface depends on its capillary pressure, which resists the wetting state transition. The anisotropic pattern of grooves naturally affects the contact line motion of a droplet, particularly during the spreading and receding phases. Therefore, directional behaviors of the spreading and receding diameter and temporal characteristics were also experimentally examined. Temporal characteristics of smooth surfaces are nearly identical to those in the direction parallel to the grooved surface, while distinctive characteristics were observed in the perpendicular direction. This discrepancy probably originated from the discontinuity of the contact line experienced in the perpendicular direction.

Graphic abstract

- Wetting state and the directional behaviors were experimentally examined.
- Surfaces exhibits periodic microscale grooves with various groove widths.
- The impalement transition to the Wenzel from Cassie state is observed from the impacting droplet.
- Directional wettability is clearly identified with the temporal diameter of droplets.
- The spreading lasts longer and reaches further in the direction parallel to the groove.

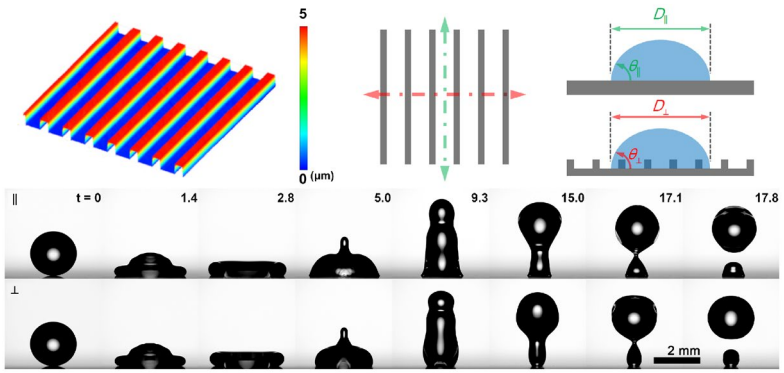

List of symbols

C	Speed of sound inside drops (m s^{-1})
D	Diameter of droplets (mm)
Oh	Ohnesorge number

✉ Eunseop Yeom
esyeom@pusan.ac.kr

Extended author information available on the last page of the article

P_C Capillary pressure (kPa)
P_D Dynamic pressure (kPa)
P_{WH} Water hammer pressure (kPa)
P_{wet} Wetting pressure (kPa)
V Impact speed (m s^{-1})
We Weber number
b Ridge width (μm)
h Groove depth (μm)
k Empirical constant for water hammer pressure
l_C Capillary length (mm)
r Roughness factor
t_s Spreading time (ms)
w Groove width (μm)
β Spreading factor
θ Contact angle (°)
μ Viscosity (mPa s)
ρ Density (kg m^{-3})
σ Surface tension (mN m^{-1})
ϕ Texture area fraction

1 Introduction

Bio-inspired surfaces such as those of plant leaves exhibiting complex topologies have been widely studied owing to their unique wetting characteristics (Koch et al. 2008). A unique characteristic is superhydrophobicity, which is fundamentally attributed to surface roughness where liquids exhibit two different wetting states. One is the Cassie–Baxter (Cassie or fakir) state (Cassie and Baxter 1944) and the other is the Wenzel state (Wenzel 1936). In the Cassie state, the liquid rests on top of the roughness features, whereas the liquid flows on the roughness features in the Wenzel state. The Cassie state has been considered to be favorable for superhydrophobic surfaces because of its higher contact angle (CA) and lower CA hysteresis compared to those of the Wenzel state (He et al. 2004). Therefore, robustness of water repellency depends on the stability of the Cassie state.

From the surface topology and intrinsic wettability of the material that forms it, an energetically stable state can be analytically determined (Lafuma and Quéré 2003). However, in numerous experimental reports, the Cassie state was observed even in the regime where the Wenzel state was stable (Öner and McCarthy 2000; Yoshimitsu et al. 2002). The transition from this Cassie state to the Wenzel state is hindered by an energy barrier (Patankar 2004). The system has to pass through a higher intermediate energy state. Hence, the system requires an additional energy source. Furthermore, even in the Cassie regime, irreversible transition to the Wenzel state can occur if a sufficient amount of energy is supplied to the system. This metastable character of the Cassie state was previously reported (Reyssat et al. 2008).

A type of additional energy, which can trigger impalement transition, arises from the drop impact. At the point of initial contact between an impinging droplet and a surface, the contact induces water hammer pressure P_{WH} (Field et al. 2012). After the contact phase, the pressure of the droplet is decreased to dynamic pressure P_D (Engel 1955; Field 1999). These two pressures are called wetting pressure P_{wet}. On the rough surface, however, there is a pressure, which resists the impalement transition. This anti-wetting pressure is called capillary pressure P_C. This is because the origin of the anti-wetting pressure is the capillary force along the contact line of the liquid and the roughness features (Jung and Bhushan 2008). Thus, the wetting state of an impinging drop depends on the balance between P_{wet} and P_C. Given that numerous solid–liquid interactions accompany the impact process, the wetting state of an impinging droplet is noteworthy.

Apart from water repellency, directional wettability is another primary wetting character of bio-surfaces, which is frequently simulated and investigated (Bixler and Bhushan 2012; Lee et al. 2013). This directionality originates from the anisotropic arrangement of surface roughness (Koch et al. 2008). Simple geometries such as periodic grooves induce directional wettability and water repellency (Vaikuntanathan and Sivakumar 2016; Guo et al. 2018). For an impinging droplet, anisotropy has been mainly observed in the spreading phase. Differences exist in the spreading characteristics of the drop measured at two primary orientations, i.e., perpendicular and parallel to the groove direction.

One difference between the two primary directions can be found in spreading factor β and ratio of the spreading diameter D to the initial value D_0, which reflects the ability of deformation during impact. This factor is important for understanding the dynamic aspect of the solid–liquid interface. The maximum spreading diameter D_m is a direct measure of the maximum solid–liquid contact area. It is examined in the normalized form called the maximum spreading factor $\beta_m = D_m/D_0$. On the surfaces with grooves, the value of β_m parallel to the groove is larger than that of β_m perpendicular to the groove (Vaikuntanathan and Sivakumar 2016; Guo et al. 2018). In addition, the spreading ends sooner in the perpendicular direction (Pearson et al. 2012). These anisotropic features have the potential to overcome the axisymmetric limitation of the drop impact in a surface-tension-dominated regime.

As mentioned earlier, superhydrophobic and directional properties can be obtained simultaneously by simply forming grooves on a surface when its intrinsic wettability is hydrophobic (i.e., CA > 90°) (Lafuma and Quéré 2003). Until now, few experimental examinations have been performed on the anisotropic behaviors of grooved surfaces. Considering the numerous surface materials available and the geometric variation of the groove, directional behaviors should be inspected in detail. Especially, dynamic behaviors

with respect to time should be investigated quantitatively for a better understanding of the impact process on anisotropic surfaces. However, the temporal variation of diameter with respect to anisotropic characteristic has been reported in a few studies only and is limited to several impact cases with a relatively low precision of measurements (Kannan and Sivakumar 2008). Furthermore, the wetting state based on P_{wet} and P_C of anisotropic surfaces with periodic grooves has not been experimentally investigated along with the anisotropic behaviors. Therefore, in this study, the wetting state and anisotropic behaviors of impacting droplets on microgrooved polymer surfaces were experimentally investigated simultaneously. In addition, the precise measurement techniques used in this study reveal the anisotropy on the temporal characteristics with a high spatiotemporal resolution.

2 Materials and methods

Surfaces made of polydimethylsiloxane (PDMS) and with unidirectional microscale grooves were prepared for this study. We used a replica molding technique for repeated production (see "Appendix" for the detailed procedure). Surfaces were designed to have identical ridge dimensions with different groove widths of 20, 40, and 80 μm and denoted them as G_{20}, G_{40}, and G_{80}, respectively. The dimensions of the prepared surfaces were measured using a three-dimensional (3D) laser microscope (VK-9700, KEYENCE Corporation). The reconstructed 3D and optical images of the PDMS microgrooved surfaces are shown in Fig. 1a–f. The values of the breadth of the ridge b, width w, and depth h of the grooves (Fig. 1g) for each surface are listed in Table 1.

The liquid used in all our impact experiments was filtrated de-ionized (DI) water of density $\rho = 995$ kg m^{-3}, surface tension $\sigma = 72.0$ mN m^{-1}, and viscosity $\mu = 1$ mPa s. Droplets were generated from a flat needle of gauge number 32 and an outer diameter of approximately 0.23 mm. The terminal impact speed was regulated by varying the drop release height. The sizes and terminal velocities were measured for each single droplet (totally 208 drop impacts were recorded and analyzed). Size D_0 of the impinging droplets was 2.06 ± 0.02 mm. The impact speed V ranged from 0.16 to 1.19 ms^{-1}.

The entire impact process was recorded by a simple imaging system consisting of a high-speed camera (Phantom VEO710L, Vision Research Inc.), an objective lens (Plan Achromat 4X, Nikon Corporation), an optical adapter (InfiniTube™ Ultima, Infinity Photo-Optical Company), and a light-emitting diode backlight. The frame rate and exposure time were 7020 frames per second (0.14 ms for each frame) and 5 μs, respectively. To identify the anisotropic wetting behavior, recording was conducted along two primary

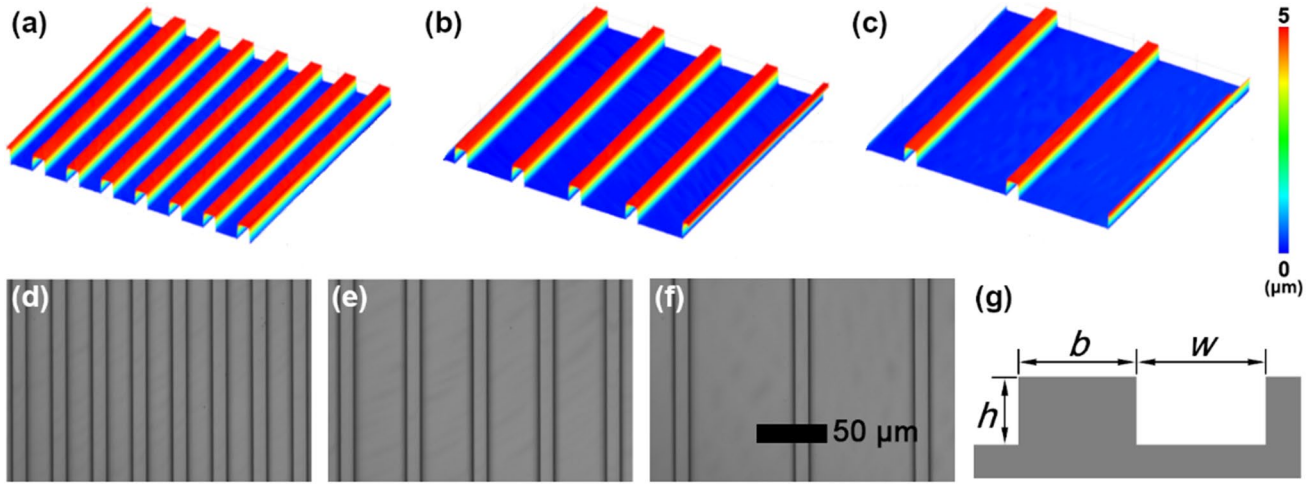

Fig. 1 Reconstructed three-dimensional schematic images of **a** G_{20}, **b** G_{40}, and **c** G_{80}; top view optical images of **d** G_{20}, **e** G_{40}, and **f** G_{80}; **g** diagram of geometric parameters

Table 1 Geometric parameters of the microgrooved surfaces and the water contact angle (CA) values estimated and measured on the microgrooved surfaces

Surface	B (μm)	W (μm)	H (μm)	ϕ	R	Theoretical CA (°)			Measured CA (°)	
						θ_W	θ_C	$\theta_{e,c}$	$\theta_{e\perp}$	$\theta_{e\parallel}$
G_{20}	10.1	19.5	4.9	0.34	1.33	98	134	132	154 ± 2	131 ± 3
G_{40}	10.0	39.1	5.3	0.20	1.22	97	145	142	157 ± 2	133 ± 2
G_{80}	10.1	78.4	5.0	0.11	1.11	96	154	152	160 ± 2	135 ± 3

directions. The quantities along (across) the groove direction are denoted by the subscript ∥ (⊥) and are called the parallel (perpendicular) quantities as shown Fig. 2b, c. The temperature and relative humidity were maintained at 24 °C and 34%, respectively, throughout the experiments. Subsequently, the recorded images were manipulated systematically using a user-designed image-processing algorithm (MATLAB Image Processing Toolbox, The MathWorks, Inc.). The diffraction limit of the optical system (~2.5 μm) is smaller than the physical dimension of the imaging plane corresponding to a pixel (~6.2 μm). Since the image-processing algorithm is based on the grayscale of pixels, the uncertainties in the length measurement are estimated to be two pixels. Considering the imaging conditions including the frame rate, the uncertainties of time, diameter, and ratio of diameters are approximately ±0.14 ms, ±0.012 mm, and ±0.017, respectively.

To verify the fundamental wettability of the prepared surfaces with DI water, we measured the water CA on the microgrooved surface prior to the impact test. For reference, we also prepared a flat and smooth surface without grooves. This flat PDMS surface and the flat portion of the microgrooved surface have a roughness value (arithmetic mean deviation, Ra) of 46 nm. The equilibrium CA θ_e on the flat and smooth surface was approximately 96 ± 1°. This corresponds to the intrinsic CA of the PDMS material used in this study. Compared to the CA measured on the microgrooved surfaces (Table 1), the apparent water repellency increased by the formation of microscale grooves. In addition, higher values of CA across the grooves, $\theta_{e\perp}$, than those along the grooves, $\theta_{e\parallel}$, were observed (Fig. 3). This anisotropic characteristic was reported experimentally (Guo et al. 2018).

The noteworthy aspect of θ_e is that both the CAs ($\theta_{e\perp}$ and $\theta_{e\parallel}$) increase as the groove width w increases. From the geometric information of the rough or structured surfaces, we can estimate the apparent CA corresponding to the wetting state of the liquid on those surfaces. The apparent CA in the Wenzel state, θ_W, is expressed as follows (Wenzel 1936):

$$\cos\theta_W = r\cos\theta_e, \tag{1}$$

where r is the roughness factor, which is the ratio of the actual surface area to the nominal projected area. For a Cassie drop, the apparent CA θ_C is expressed as follows (Cassie and Baxter 1944):

$$\cos\theta_C = \phi\cos\theta_e + \phi - 1, \tag{2}$$

where ϕ is the texture area fraction, which is defined as the proportion of the projected wet area underneath the droplet. In this study, $r = 1 + 2h/(w+b)$ and $\phi = b/(w+b)$. The values of θ_C evidently increase as w increases due to reduced ϕ (Table 1). In addition, θ_C lies between $\theta_{e\perp}$ and $\theta_{e\parallel}$. From the large gap between the values of θ_W and the measured

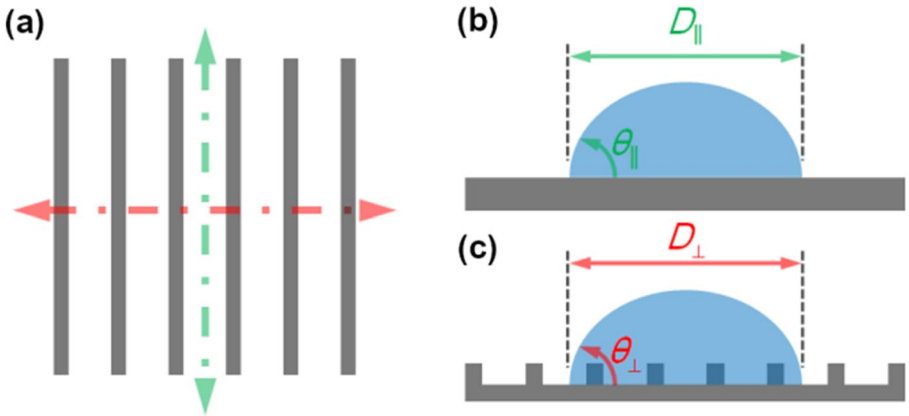

Fig. 2 Two orthogonal measurement directions with respect to the groove length direction. **a** Top view; **b** parallel quantities measured along the groove direction; **c** perpendicular quantities measured across the groove direction

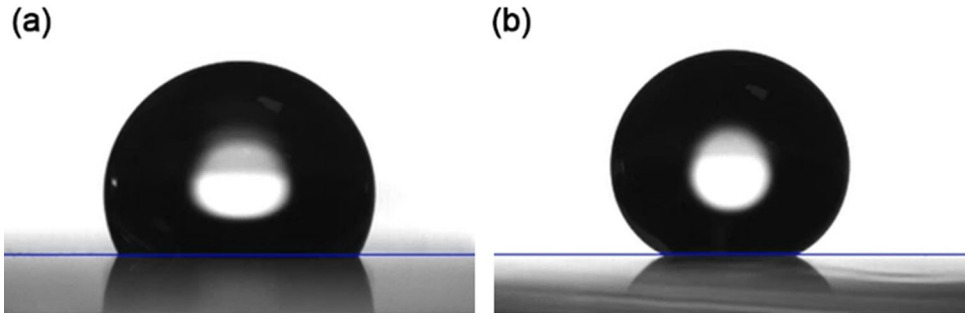

Fig. 3 Sessile drop on the G_{80} for the contact angle measurements **a** parallel, $\theta_{e\parallel}$ and **b** perpendicular, $\theta_{e\perp}$ to the groove direction. The drop volume is 5.0 μL. The base line for the measurement is indicated in blue solid line

CA, and the contrary trend with increasing w, the wetting state of the sessile droplets used for the CA measurements would be in the Cassie state.

As mentioned earlier, the energetically stable state can be analytically determined. Threshold CA $\theta_{e,c}$, which decides the lower energy state for a specified roughness, is given by equating Eqs. (1) and (2) (Bico et al. 2002):

$$\cos\theta_{e,c} = \frac{\phi - 1}{r - \phi}. \tag{3}$$

From the analytical perspective, the Cassie state is feasible when θ_e is larger than $\theta_{e,c}$. Thus, the energetically stable state of the microgrooved surfaces in this study is the Wenzel state, although the gently deposited sessile droplets are in the Cassie state.

3 Results and discussion

3.1 Wetting states of impinging droplets

The Cassie state maintained for the sessile droplets is metastable because the microstructured surfaces in this study are more stable in the Wenzel state. To determine the stability of the Cassie state (or the water repellency), the impact behaviors of impinging droplets with additional energy in the form of P_{wet} were investigated. Since the scale of the phenomena is smaller than the capillary length $l_C = \sqrt{\sigma/\rho g}$, where g is the gravitational acceleration, gravity can be neglected (de Gennes et al. 2004). The impact regime is generally introduced by the Weber number $We = \rho V^2 D_0/\sigma$ of the droplets, which scales the importance of the inertia compared to the capillary force. The viscous effect in a free surface situation can be assessed by the Ohnesorge number $Oh = \mu/\sqrt{\rho\sigma D_0}$. The We regime of the present study ranges from 0.8 to 40, as shown in Fig. 4. In most of the previous studies, We ranges are broader than that in this study. A few of these We ranges are 20–200 (Lv et al. 2016), 5–280 (Guo et al. 2018), and 1–100 (Vaikuntanathan and Sivakumar 2016). Although the impact regime is relatively narrow in this study, we provide an approximately 50% denser interval between the impact cases than that provided in previous studies.

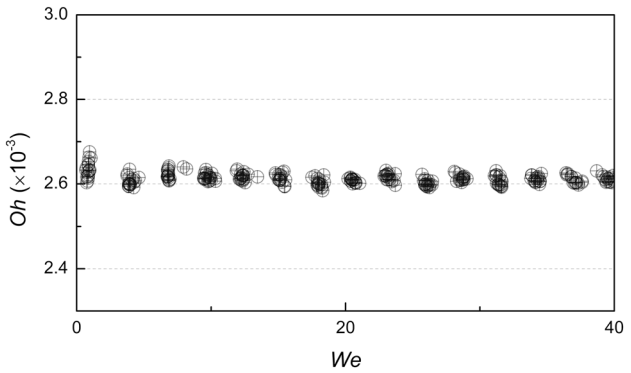

Fig. 4 Impact regime of this study represented by We and Oh of impinging droplets

On the smooth PDMS surface without grooves, liquid lamella of the impinging drop gently spreads and then recedes. Subsequently, the contact line is pinned followed by damped oscillations of the top interface. The typical impact process is depicted in Fig. 5. Bouncing does not occur on the smooth surface regardless of We. However, on G_{20}, the droplet starts to rebound from the smallest We. Two bouncing droplets with nearly same We were observed at different primary directions, as shown in Fig. 6. Each pair of images (one in each direction) is captured at identical instants from the initial contact. The contact lines do not get pinned in the receding phase and finally bounce off without remnant liquid on the surface. This is strong evidence for the enhanced water repellency of G_{20} compared to that of the smooth surface in addition to the increased θ_e discussed earlier.

The droplets with We higher than 15 exhibit sticky behaviors on G_{20}. In the receding phase, the contact line is pinned, and a part of the drop sticks to the surface as shown in Fig. 7. The pinned contact line and the remnant liquid on the surface are evidence of the impalement transition to the Wenzel state (Lafuma and Quéré 2003). To validate the wetting state transition with respect to the balance between P_{wet} and P_C, we first evaluate P_C for the surfaces used in this study. By virtue of periodic grooves, the balance between the force from the internal drop pressure and the capillary force along the contact line can be examined through the groove length as follows:

$$wP_C = 2\sigma|\cos\theta|, \tag{4}$$

where wP_C is the force applied on unit area of the free surface and $2\sigma|\cos\theta|$ is the capillary force, which resists the transition.

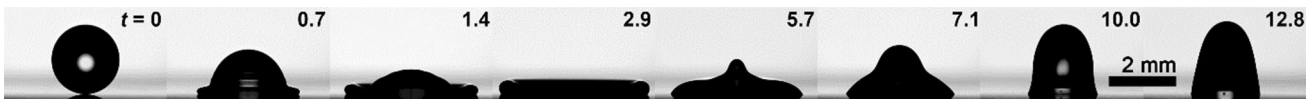

Fig. 5 Impact sequences of the water drop with $We = 34.4$ on the smooth polydimethylsiloxane (PDMS) surface. Elapsed time from the initial contact is indicated at the top right corner (in ms)

In addition, there are two distinctive mechanisms responsible for impalement transition: sag and de-pinning mechanism (refer Fig. 8) (Patankar 2004). In the sag mechanism, the liquid–air interface pinned on top of the roughness features touches the basal surface. The increased pressure inside a drop deforms the interface. Simultaneously, local CA θ (depicted in Fig. 8a) between the interface and roughness feature increases. However, this contact angle has an upper limit called the advancing contact angle θ_A. If the local contact angle exceeds the advancing angle, the pinning fails and the contact line slides downward to touch the basal surface (Fig. 8b). This is the de-pinning mechanism.

Based on the de-pinning mechanism, P_C can be conveniently evaluated by replacing θ with θ_A (110° in this study) in Eq. (4). Subsequently, P_C for de-pinning, $P_{C,depin}$, can be expressed as:

$$P_{C,depin} = 2\sigma\left|\cos\theta_A\right|/w. \tag{5}$$

To calculate P_C accurately based on the sag mechanism, $P_{C,sag}$, we require complete information of the drop. We can estimate the sag geometry by adopting a marginal-deformation approximation as adopted in previous studies (Jung and Bhushan 2007). Since groove width is significantly smaller than drop size, the curvature along the groove length direction would be negligible when compared to that in the direction perpendicular to the groove. Hence, $P_{C,sag}$ is expressed in a simple form as:

$$P_{C,sag} = \sigma/R, \tag{6}$$

where R is the radius of curvature of the interface at the touch-down moment. In addition to the values of P_C, we present the critical local CA θ_{sag}, at which the sag transition occurs, in Table 2. Since the θ_{sag} values for G_{20} and G_{40} are larger than θ_A in this study, impalement transitions on G_{20} and G_{40} will occur through the de-pinning mechanism.

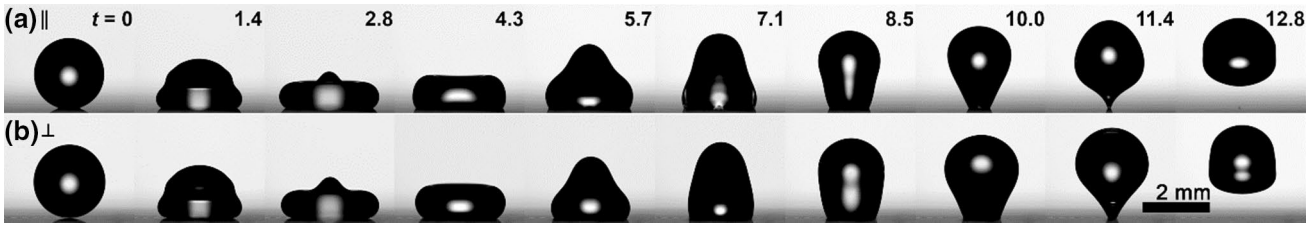

Fig. 6 Drop impact sequences on the G_{20}. **a** The droplet with $We = 3.94$ is imaged at the parallel direction; **b** the droplet with $We = 3.96$ is imaged at the perpendicular direction. At each pair of images for two directions, elapsed time from the initial contact is indicated at the top right corner (in ms)

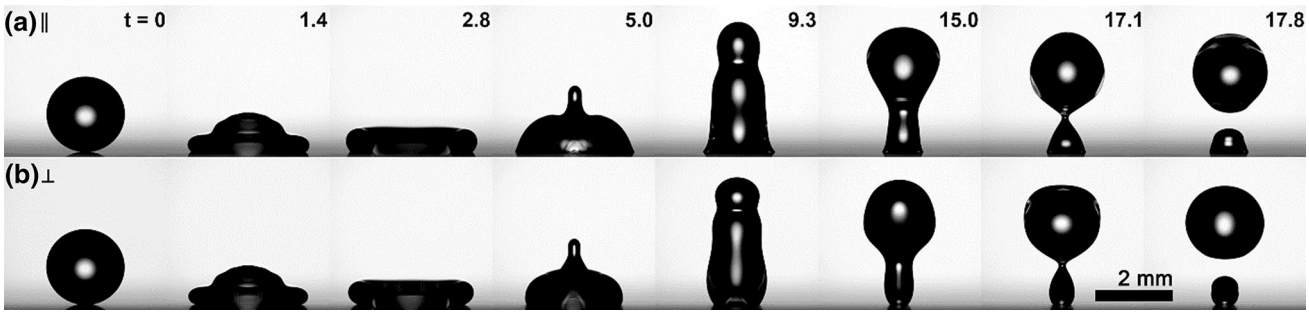

Fig. 7 Impact sequences of the droplets having the same $We = 15.2$ on the G_{20}. Images recorded at the **a** parallel and **b** perpendicular direction, respectively. At each pair of images for two directions, elapsed time from the initial contact is indicated at the top right corner (in ms)

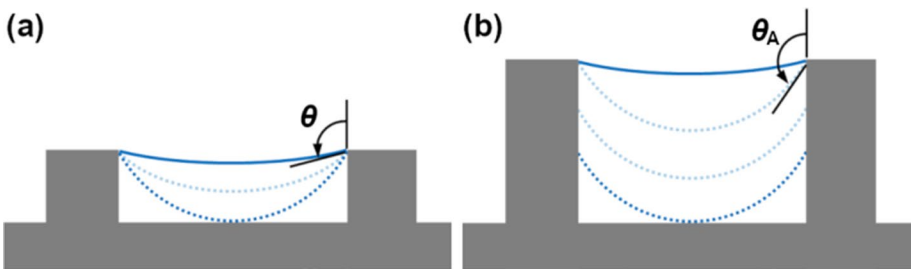

Fig. 8 Schematic diagrams (side view) of the impalement transition corresponding to **a** sag mechanism and **b** de-pinning mechanisms. The solid (dotted) line indicates the interface of the drop in the Cassie state (in transition)

Table 2 The critical local contact angle θ_{sag} at which the sag transition occurs and the capillary pressure P_C corresponding to the sag $P_{C,sag}$ and de-pinning mechanisms $P_{C,depin}$

Surface	θ_{sag} (°)	$P_{C,sag}$ (kPa)	$P_{C,depin}$ (kPa)
G_{20}	143	5.93	2.53
G_{40}	120	1.86	1.26
G_{80}	105	0.46	0.63

As mentioned earlier, the wetting pressures of an impinging droplet comprise of $P_D = 0.5\rho V^2$ and $P_{WH} = k\rho CV$, where k is a constant, which depends on the impact conditions, and C is the sound speed of the droplet (Engel 1955; Field 1999). Since P_{WH} is applied to a very confined area (Field 1991) and is released in the early stage of contact, P_{WH} and P_D were evaluated separately at the contact and spreading stages, respectively (Deng et al. 2009). In this study, this two-stage approach was applied and coefficient k was determined to ensure that wetting pressures for the drops leaving the remnant liquid after bouncing exceed P_C. Since remnant liquid is the evidence of impalement transition, one of the wetting pressures must be larger than P_C. The possible range of k, which makes P_{WH} satisfy the condition for impalement transition, can be determined for the droplet whose P_D is smaller than P_C. The range of k narrowed down to a specific value as the examination proceeded toward the impact cases with three different values of P_C. It is noteworthy that coefficient k has been usually determined empirically for textured surfaces (Kwon et al. 2013; Maitra et al. 2014). These empirical values are usually two orders of magnitude smaller than the values based on the analytic processes on flat surfaces ($k = 0.2$) (Engel 1955). In this study, k is 0.0025, which is two orders of magnitude smaller than 0.2. It is interesting to note that some researchers treated P_D and P_{WH} together (Maitra et al. 2014). In this one-stage approach, P_C is balanced with $P_D + P_{WH}$. In addition, the dependency of k on P_C has been reported in other experimental studies (Dash et al. 2012). Clear differences exist among the experimental studies on P_{WH} and k. Hence, it is necessary to study them in the near future.

The resultant pressure map from $k = 0.0025$ is presented in Fig. 9. For all the impact cases on G_{20}, P_D is lower than P_C. However, P_{WH} exceeds P_C for the droplets with *We* higher than 15. When P_{WH} solely exceeds P_C, a narrow portion around the initial contact point of the area underneath the drop wets the roughness. This partial impalement occurs because P_{WH} acts on the initial contact point for a very short period (Hyväluoma and Timonen 2008). As *We* or P_{WH} is further increased, the amount of remnant liquid stuck to the surface increases because the liquid volume that penetrates the grooves increases (Fig. 10). All the microgrooved surfaces in this study display an identical trend.

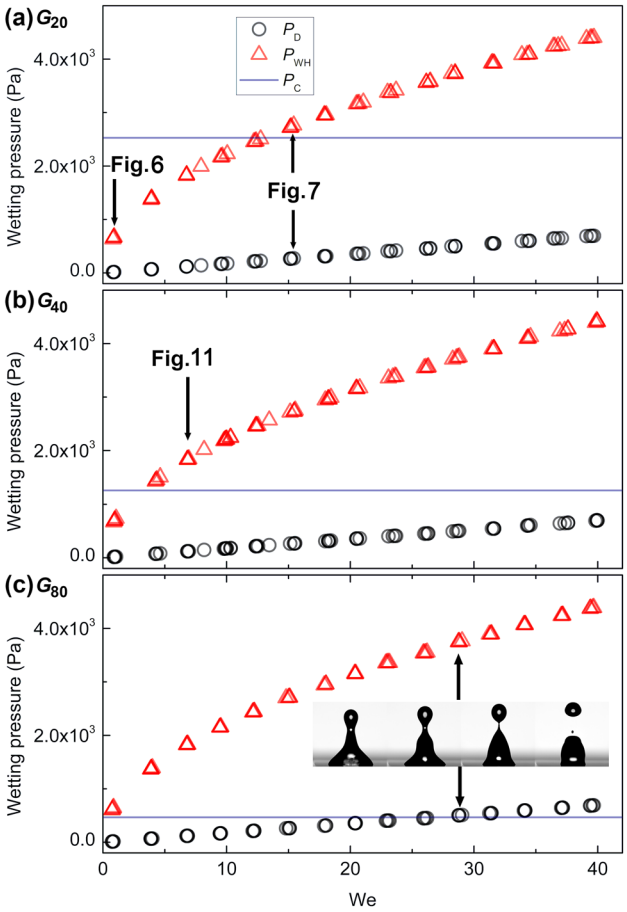

Fig. 9 Wetting pressure P_{wet} of impinging droplets are presented with their *We* on **a** G_{20} having the P_C of 2.53 kPa, **b** G_{40} having the P_C of 1.26 kPa, and **c** G_{80} having the P_C of 0.46 kPa. The data points corresponding to impact sequence figures are denoted. The inset images display the receding phase of the impacting drop with $We = 28.8$ recorded at the parallel direction

On the microgrooved surface G_{40}, P_{WH} starts to exceed P_C when *We* is approximately five (Fig. 9). The sticky behaviors from the partial impalement of the impinging droplets with *We* of approximately seven are depicted in Fig. 11. The decreased water repellency is directly identifiable from the lower value of P_C for G_{40} than that for G_{20}. On G_{80} with the lowest value of P_C, all the impact cases undergo impalement transition. Furthermore, both the P_{wet} values exceed P_C as *We* of the impacting droplets reach approximately 28. However, no special difference is observed, as depicted in the inset of Fig. 9c. It should be noted that the apparent CA measured on G_{80} is the highest among the three microgrooved surfaces, whereas P_C and the resulting water repellency are the lowest. Therefore, we consider that the degree of hydrophobicity cannot be evaluated by CA alone, at least for these types of one-tier roughness surfaces.

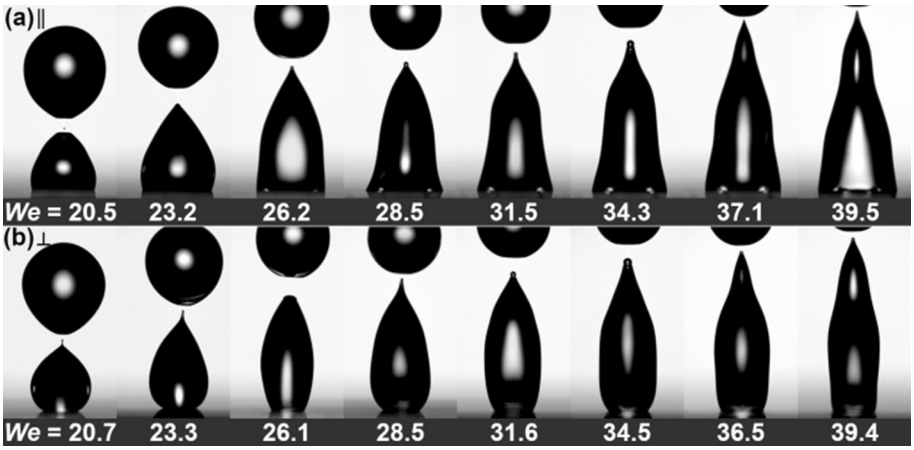

Fig. 10 The remnant liquids stick to the surface G_{20} imaged at the **a** parallel and **b** perpendicular directions. Images are captured right after the detachment of the main drop. *We* corresponding to each impact case is denoted below

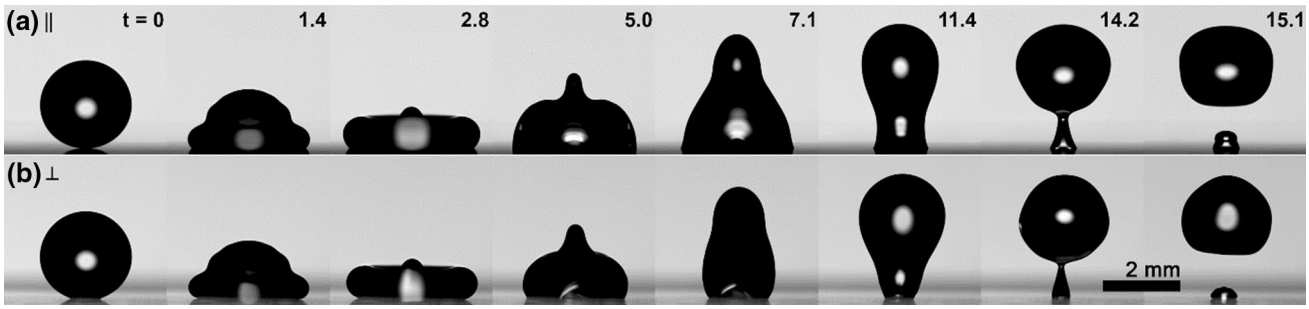

Fig. 11 Drop impact sequences on the G_{40}. **a** The droplet with $We = 6.83$ is imaged at the parallel direction; **b** the droplet with $We = 6.89$ is imaged at the perpendicular direction. At each pair of images for two directions, elapsed time from the initial contact is indicated at the top right corner (in ms)

3.2 Directional wetting characteristics

As is apparent from the impact sequences (Figs. 5, 6, 10), the shape of a drop, particularly the length of contact line and CA, is distinguishable between the parallel and perpendicular directions. To assess directional wettability, we precisely measure temporal variations of the spreading and receding diameters. As shown in Fig. 12, the diameters D over time on G_{80} are compared to those on the smooth surface. For better visibility, we present only the diameters of the selected droplets with relatively high *We*. On the smooth surface, the spreading diameters increase with time until they reach D_m as shown in Fig. 12a. The diameter of the drop with higher *We* is greater than that with lower *We* throughout the spreading and receding phases. The gap between the values of the diameters with respect to *We* reaches its maximum at the time of D_m and gradually decreases in the receding phase. A similar tendency with respect to time and the value itself can be found from the D measured along the groove direction on G_{80} (Fig. 12b).

Dynamic behavior of the D measured perpendicular to the groove (Fig. 12c) is distinguished from others especially in the receding phase. Although the decreasing rate temporarily falls off about 1 ms after the beginning of the receding phase, it is insignificant to the overall receding rate. However, as shown in Fig. 12a, b, receding begins with a relatively slow rate, which decreases rapidly about 3 ms later. In this study, the log–log plots of the spreading factor β are given in the inset images to reveal the quantitative difference in the dynamic receding of diameters. On the smooth and G_{80} surfaces measured in the parallel direction, there are two distinct regions with two different scaling exponents in the receding phase. Regardless of the existence of microgrooves, the values of scaling power of each region coincide (-0.1 and -0.7). In contrast, the spreading factor measured perpendicular to the groove on G_{80} is scaled as $\beta \sim t^{-1.6}$ throughout the receding phase. Previously, the relationship between the dynamic receding diameter and time was scaled as $\beta \sim t^{-1}$ on microtextured surfaces (Lv et al. 2016). The power of scaling was fixed to -1. The surfaces were covered with an isotropic array of microscale posts. Previous studies on the receding dynamics of smooth surfaces differ from the present study without anisotropy. However, they are similar for microgrooved surfaces measured across the grooves. We consider that this similarity comes from the discontinuity experienced by the contact line across the groove direction

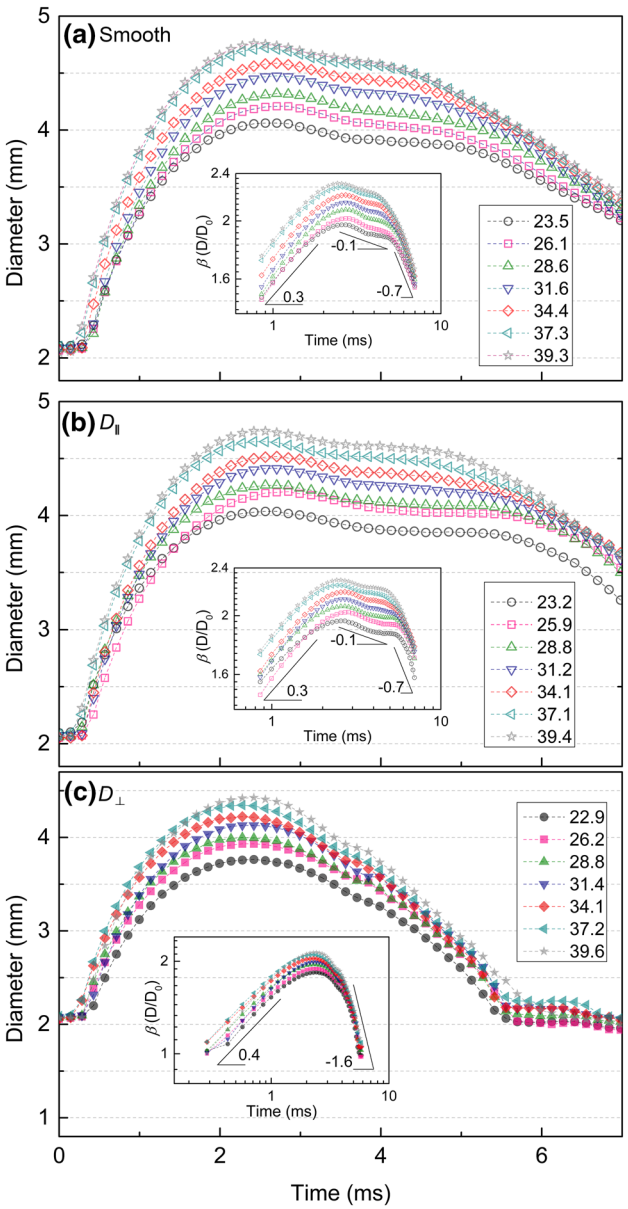

Fig. 12 Temporal variations of the drop diameters after impact on the **a** smooth surface, and G_{80} measured in the **b** parallel and **c** perpendicular directions. The values of *We* for each impact case are denoted. Scaling law analyses for the spreading factors are presented in the inset

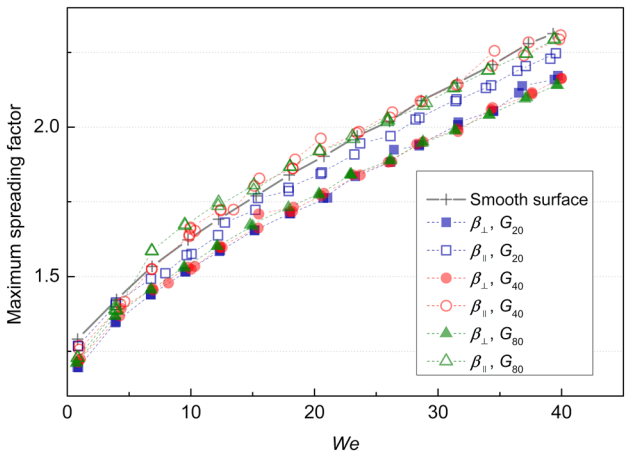

Fig. 13 The maximum spreading factors β_m on the smooth surface and the microgrooved surfaces. The filled (hollow) symbols indicate the β_m measured perpendicular (parallel) to the groove direction

because this discontinuity would be experienced on the isotropic pillar array in any direction.

Among the studies on the spreading and receding dynamics on grooved surfaces, Kannan and Sivakumar (2008) reported that $D_{\parallel}$ followed a tendency similar to that observed for smooth surfaces such as the surface used in this study. $D_{\perp}$ showed two different receding rates, and the first rate was significantly slower than the second. Interestingly, this was observed on the smooth surface and the G_{80} measured parallel to the grooves ($D_{\parallel}$) in the present study. Certain differences in the experimental conditions between both the studies exist. However, such differences are not significant enough to affect the trend, and the clear cause for the opposing trend of the receding phase according to the measurement direction requires further study. The groove scale considered in the study by Kannan and Sivakumar (2008) was an order of magnitude higher than that in the present study. In addition, only three values of *We* were given in the previous study (48, 82, and 169). Moreover, the receding diameter on the smooth surface for $We = 42$ showed an opposing behavior to the arguments of the previous study. It actually showed two distinctive regions with several milliseconds of relatively insignificant changes.

The abovementioned anisotropic characters are prevalent among the microgrooved surfaces in this study observed from the maximum spreading factor β_m of all the surfaces, as shown in Fig. 13. For all the microgrooved surfaces, β_m measured perpendicular to the groove direction, $\beta_{m\perp}$, is smaller than that measured parallel to the groove, $\beta_{m\parallel}$. The difference between them is visible when *We* increases. For a given *We*, the values of $\beta_{m\parallel}$ on grooved surfaces are similar to that on the smooth surface. This property is consistent with that mentioned in previous studies addressing surfaces with grooved patterns (Kannan and Sivakumar 2008; Vaikuntanathan and Sivakumar 2016; Guo et al. 2018). Furthermore, the authors of the previous studies concluded that pinning of a drop on the pillar top and impalement transition hinder the spreading of the drop liquid perpendicular to the groove. In this study, the values of $\beta_{m\perp}$ are closely gathered for a given *We,* whereas the values of $\beta_{m\parallel}$ are relatively dispersed. This is probably due to limited contact line motion across the groove. However, this type of discontinuous motion of the contact line requires an analysis of the flow inside the

drop (Liu and Chen 2017). Thus, a study on the underlying mechanism of this phenomenon would be an effective topic for future study if suitable techniques to measure the flow inside a drop were available.

Another aspect of anisotropy is apparent in the spreading time, t_s, of the impinging droplet. In Fig. 14, t_s on the smooth surface, G_{40}, and G_{80} are presented. In this study, the t_s measured perpendicular to the groove is shorter than that measured parallel to the groove regardless of the groove width. This implies that spreading along the groove direction continues after the end of spreading in the perpendicular direction. This indicates the highly complex and asymmetric flow inside the droplet during the spreading phase. Except for this directional property, the overall trends are reasonably consistent with those of the previous reports. t_s has been revealed to be independent of the impact velocity (Okumura et al. 2003; Clanet et al. 2004). Moreover, it has been reported that t_s increases as the impact velocity decreases only when the impact velocity is significantly low (Okumura et al. 2003). In this study, t_s is almost invariant as *We* exceeds approximately 10.

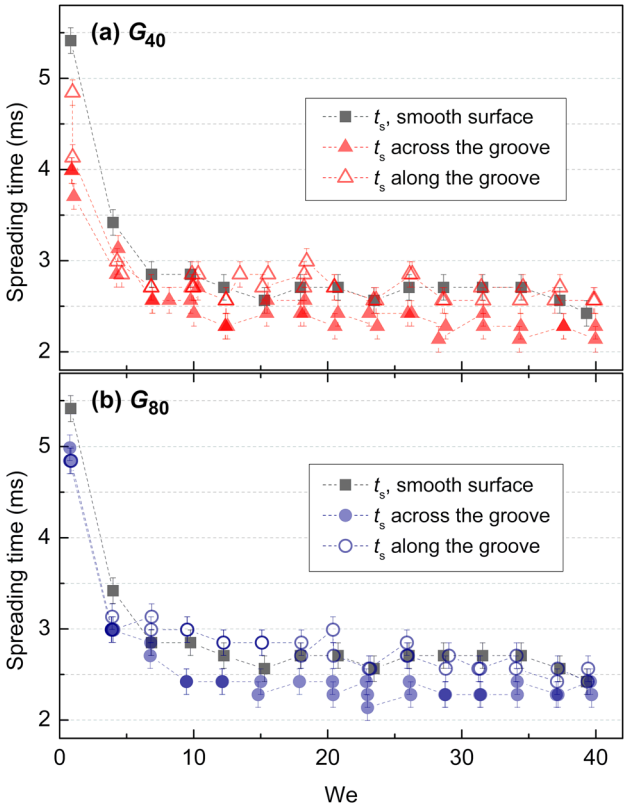

Fig. 14 The spreading time t_s of the droplets impact on **a** G_{40} and **b** G_{80}. The filled (hollow) symbols indicate the t_s measured perpendicular (parallel) to the groove direction

4 Conclusions

In this study, we experimentally examine the wetting state and directional behaviors of microgrooved PDMS surfaces. The application of microscale texture dramatically changes the wettability of the surfaces. For impinging droplets, water repellency of the surfaces is greatly increased. Drop impact experiments show that the ability to resist liquid impalement is determined by the P_C of the surface. Therefore, G_{20} with the shortest groove width and largest P_C exhibits the best water-repellent performance. It is noteworthy that CA is no more a relevant parameter for assessing water repellency, although it has been conventionally regarded as a measure of superhydrophobicity. This corresponds to the experimental result that all the impact cases on G_{80} leave remnant liquid on the surface, while the measured and estimated CA on G_{80} is the greatest. Another wetting characteristic arising from the groove pattern is the anisotropic variation of spreading and receding during impact. The D measured on the smooth surface and $D_{\parallel}$ behave alike, showing two steps of receding. It should be noted that the receding diameter was scaled with a single decaying exponent (Lv et al. 2016). However, we believe that elaborate data acquisition with a fine resolution in this study reveals the actual characteristic of the receding phase. In fact, $D_{\perp}$ decreases faster with a single decaying exponent. This directional wettability is supported by consistent and vast experimental data. Thus, we consider that this study resolves ambiguous directional properties found in a previous study (Kannan and Sivakumar 2008).

Acknowledgements This work was supported by the National Research Foundation of Korea (NRF) Grant funded by the Korea government (MSIP) (NRF-2019R1H1A1079157).

Appendix: Replica molding procedure

The Si mold master was fabricated via a conventional photolithography method. The master was coated with a self-assembled monolayer (SAM) for repeated use and a smooth mold surface. The SAM coating procedure is as follows:

1. Reduce the humidity in the desiccator chamber to below 30% by desiccants (moisture absorbing particles).
2. Load the Si master in the desiccator chamber.
3. Load a 0.7-μL solution of heptadecafluoro-1,1,2,2-tetrahydrodecyl-trichlorosilane (HDFS, Gelest) on the Teflon plate.
4. Incubate for 48 h.
5. Unload the Si master and immediately clean it with *n*-hexane.
6. Rinse the Si master with DI water and blow with N_2 gas.

After coating SAM on the master surface, the following replica molding procedure is followed:

1. Mix the polymer base with the curing agent (10:1 weight to weight).
2. Pour PDMS onto the Si master.
3. Degas the poured PDMS under 0.9 bar for 30 min.
4. Thermally cure the degassed PDMS for 20 min at 100 °C.
5. Peel off the cured PDMS from the Si master.

References

Bico J, Thiele U, Quéré D (2002) Wetting of textured surfaces. Coll Surf A Physicochem Eng Asp 206:41–46. https://doi.org/10.1016/S0927-7757(02)00061-4

Bixler GD, Bhushan B (2012) Bioinspired rice leaf and butterfly wing surface structures combining shark skin and lotus effects. Soft Matter 8:11271. https://doi.org/10.1039/c2sm26655e

Cassie ABD, Baxter S (1944) Wettability of porous surfaces. Trans Faraday Soc 40:546. https://doi.org/10.1039/tf9444000546

Clanet C, Béguin C, Richard D, Quéré D (2004) Maximal deformation of an impacting drop. J Fluid Mech 517:199–208. https://doi.org/10.1017/S0022112004000904

Dash S, Alt MT, Garimella SV (2012) Hybrid surface design for robust superhydrophobicity. Langmuir 28:9606–9615. https://doi.org/10.1021/la301743p

de Gennes P-G, Brochard-Wyart F, Quéré D (2004) Capillarity and wetting phenomena. Springer, New York

Deng T, Varanasi KK, Hsu M et al (2009) Nonwetting of impinging droplets on textured surfaces. Appl Phys Lett 94:133109. https://doi.org/10.1063/1.3110054

Engel OG (1955) Waterdrop collisions with solid surfaces. J Res Natl Bur Stand (1934) 54:281. https://doi.org/10.6028/jres.054.033

Field JE (1991) The physics of liquid impact, shock wave interactions with cavities, and the implications to shock wave lithotripsy. Phys Med Biol 36:1475–1484

Field JE (1999) ELSI conference: invited lecture liquid impact: Theory, experiment, applications. Wear 233–235:1–12

Field JE, Camus J-J, Tinguely M et al (2012) Cavitation in impacted drops and jets and the effect on erosion damage thresholds. Wear 290–291:154–160. https://doi.org/10.1016/j.wear.2012.03.006

Guo C, Zhao D, Sun Y et al (2018) Droplet impact on anisotropic superhydrophobic surfaces. Langmuir 34:3533–3540. https://doi.org/10.1021/acs.langmuir.7b03752

He B, Lee J, Patankar NA (2004) Contact angle hysteresis on rough hydrophobic surfaces. Coll Surf A Physicochem Eng Asp 248:101–104. https://doi.org/10.1016/j.colsurfa.2004.09.006

Hyväluoma J, Timonen J (2008) Impalement transitions in droplets impacting microstructured superhydrophobic surfaces. Europhys Lett 83:64002. https://doi.org/10.1209/0295-5075/83/64002

Jung YC, Bhushan B (2007) Wetting transition of water droplets on superhydrophobic patterned surfaces. Scr Mater 57:1057–1060. https://doi.org/10.1016/j.scriptamat.2007.09.004

Jung YC, Bhushan B (2008) Dynamic effects of bouncing water droplets on superhydrophobic surfaces. Langmuir 24:6262–6269. https://doi.org/10.1021/la8003504

Kannan R, Sivakumar D (2008) Drop impact process on a hydrophobic grooved surface. Coll Surf A Physicochem Eng Asp 317:694–704. https://doi.org/10.1016/j.colsurfa.2007.12.005

Koch K, Bhushan B, Barthlott W (2008) Diversity of structure, morphology and wetting of plant surfaces. Soft Matter 4:1943. https://doi.org/10.1039/b804854a

Kwon DH, Huh HK, Lee SJ (2013) Wetting state and maximum spreading factor of microdroplets impacting on superhydrophobic textured surfaces with anisotropic arrays of pillars. Exp Fluids 54:1576. https://doi.org/10.1007/s00348-013-1576-5

Lafuma A, Quéré D (2003) Superhydrophobic states. Nat Mater 2:457–460. https://doi.org/10.1038/nmat924

Lee SG, Lim HS, Lee DY et al (2013) Tunable anisotropic wettability of rice leaf-like wavy surfaces. Adv Funct Mater 23:547–553. https://doi.org/10.1002/adfm.201201541

Liu M, Chen XP (2017) Numerical study on the stick-slip motion of contact line moving on heterogeneous surfaces. Phys Fluids 29:082102

Lv C, Hao P, Zhang X, He F (2016) Drop impact upon superhydrophobic surfaces with regular and hierarchical roughness. Appl Phys Lett 108:141602. https://doi.org/10.1063/1.4945662

Maitra T, Tiwari MK, Antonini C et al (2014) On the nanoengineering of superhydrophobic and impalement resistant surface textures below the freezing temperature. Nano Lett 14:172–182. https://doi.org/10.1021/nl4037092

Okumura K, Chevy F, Richard D et al (2003) Water spring: a model for bouncing drops. Europhys Lett 62:237–243. https://doi.org/10.1209/epl/i2003-00340-1

Öner D, McCarthy TJ (2000) Ultrahydrophobic surfaces. Effects of topography length scales on wettability. Langmuir 16:7777–7782. https://doi.org/10.1021/la000598o

Patankar NA (2004) Transition between superhydrophobic states on rough surfaces. Langmuir 20:7097–7102. https://doi.org/10.1021/la049329e

Pearson JT, Maynes D, Webb BW (2012) Droplet impact dynamics for two liquids impinging on anisotropic superhydrophobic surfaces. Exp Fluids 53:603–618. https://doi.org/10.1007/s00348-012-1320-6

Reyssat M, Yeomans JM, Quéré D (2008) Impalement of fakir drops. Europhys Lett 81:26006. https://doi.org/10.1209/0295-5075/81/26006

Vaikuntanathan V, Sivakumar D (2016) Maximum spreading of liquid drops impacting on groove-textured surfaces: effect of surface texture. Langmuir 32:2399–2409. https://doi.org/10.1021/acs.langmuir.5b04639

Wenzel RN (1936) Resistance of solid surfaces to wetting by water. Ind Eng Chem 28:988–994. https://doi.org/10.1021/ie50320a024

Yoshimitsu Z, Nakajima A, Watanabe T, Hashimoto K (2002) Effects of surface structure on the hydrophobicity and sliding behavior of water droplets. Langmuir 18:5818–5822. https://doi.org/10.1021/la020088p

Publisher's Note Springer Nature remains neutral with regard to jurisdictional claims in published maps and institutional affiliations.

Affiliations

Daehee Kwon[1] · Sangmin Lee[2] · Eunseop Yeom[3]

Daehee Kwon
fledgent@postech.ac.kr

Sangmin Lee
thinking@deu.ac.kr

[1] Corporate Research and Development Center, Samsung Electro-mechanics, 150, Maeyeong-ro, Yeongtong-gu, Suwon-si, Gyeonggi-do, Republic of Korea

[2] Division of Mechanical Automotive, Robot Components Engineering (Automotive Major), Dong-Eui University, 176, Eomgwang-ro, Busanjin-gu, Busan 47340, Republic of Korea

[3] School of Mechanical Engineering, Pusan National University, 2, Busandaehak-ro 63beon-gil, Geumjeong-gu, Busan 46241, Republic of Korea